objective function is nonlinear, and the constraint is linear. The fundamental frequency was increased from 212.554 rad/s to 218.225 rad/s. The optimal flange-thickness distribution followed the pattern of the bending-moment distribution corresponding to the fundamental mode of vibration.

Cantilever Beam

Next, cantilever-end conditions were considered. First, the volume of the beam was minimized with single and multiple frequency constraints. The fundamental frequency of the beam at the initial design was 72.465 rad/s. The volume was minimized subject to a fundamental frequency constraint of $\omega_1 \geq 75.0$ rad/s. The total volume of the beam was reduced 33% – from 2.7 in.^{3} at the initial design to 1.80 in.^{3} at the optimum design. The optimal flange-thickness distribution is shown in Fig. 4. The optimal flange-thickness distribution has a maximum at the support with a minimum at the free end of the beam. The optimal flange-thickness distribution followed the pattern of the bending moment distribution corresponding to the fundamental mode of vibration.

Next, the volume of the cantilever beam was minimized subject to multiple frequency constraints. The volume minimization problem was posed with three frequency constraints of $\omega_1 \geq 75.0$ rad/s, $\omega_2 \geq 120.0$ rad/s, and $\omega_3 \geq 140.0$ rad/s. The total volume was reduced to 1.91 in.^{3}. The first three natural frequencies at the optimum design were $\omega_1 = 75.0$ rad/s, $\omega_2 = 122.039$ rad/s, and $\omega_3 = 140.0$ rad/s. The first and third constraints were satisfied as equality constraints even though they were posed as inequality constraints. The optimal flange thickness distribution was similar to the one obtained for the single constraint case.

Finally, the cantilever beam was designed for the fundamental frequency maximization with a constraint on the total volume of the beam. The fundamental frequency was increased from 72.465 rad/s to 99.862 rad/s. The optimal flange thickness distribution assumes a maximum at the support and a minimum at the free end of the beam.

Conclusions

In this paper, optimum design of beams vibrating in coupled bending and torsion was considered. The selection of the lower limit on design variables is important to prevent the switching of the shear center location with respect to the centroid during the progress of optimization. Optimum-thickness distributions and design-iteration histories were presented for the simply supported and cantilever beams with rectangular box cross section. The optimal flange-thickness distribution followed the pattern of the dominant mode of vibration.

Acknowledgment

This research work was partially supported by the Wright Research and Development Center at Wright Patterson Air Force Base, Ohio, and the State of Ohio Research Challenge Program.

References

[1]Peters, D. A., Ko, T., Korn, A., and Rossow, M. P., "Design of Helicopter Rotor Blades for Desired Placement of Natural Frequencies," *Proceedings of the 39th Annual Forum of the American Helicopter Society,* American Helicopter Society, May 1983.

[2]Chattopadhyay, A., Hanagud, S. V., and Smith, C. V., Jr., "Minimum Weight Design of a Structure with Dynamic Constraints and A Coupling of Bending and Torsion," *Proceedings of the AIAA/ASME/ASCE/AHS 27th Structures, Structural Dynamics, and Materials Conference,* AIAA-CP-86-0928, Part 2, AIAA, New York, 1986, pp. 386–394.

[3]Hanagud, S., Smith, C. V., Jr., and Chattopadhyay, A., "Optimal Design of a Vibrating Beam with Coupled Bending and Torsion," *AIAA Journal*, Vol. 25, No. 9, 1987, pp. 1231–1240.

[4]Grandhi, R. V., and Moradmand, J. K., "Optimum Synthesis of Thin-Walled Vibrating Beams with Coupled Bending and Torsion," *Journal of Mechanisms, Transmissions, and Automation in Design*, Vol. 3, No. 4, 1989, pp. 555–560.

[5]Timoshenko, S. P., and Goodier, N. J., *Theory of Elasticity*, 3rd ed., McGraw-Hill, New York, 1970.

[6]Grandhi, R. V., Thareja, R. T., and Haftka, R. T., "NEWSUMT – A: A General Purpose Program for Constrained Optimization Using Constraint Approximations," *ASME Journal of Mechanisms, Transmissions, and Automation Design*, Vol. 107, 1985, pp. 94–99.

Low-Speed Pressure Distribution on Semi-Infinite Two-Dimensional Bodies with Elliptical Noses

Erik S. Larson*
FFA, The Aeronautical Research Institute of Sweden, Bromma, Sweden

Introduction

In a recent Note,[1] a semiempirical representation of the pressure distribution on ellipsoids of revolution and elliptic-nosed, semi-infinite bodies of revolution in axial, incompressible flow was constructed by taking the lead from early theoretical results.[2,3] A similar approach is applied to a family of semi-infinite, two-dimensional bodies with elliptical noses in symmetric, incompressible flow, for which Hess and Smith[3] have presented numerical solutions of the potential flow equations. As could be expected, the same type of expressions that appeared as in the axial flow case, after modification of some constants and exponents, gave a very good representation of the theoretical results for nose slenderness ratios up to unity. The pressure drag of the noses was to be determined by numerical integration.

Analytic Expressions

Elliptic Profiles

The analytic expression for the pressure distribution on ellipsoids of revolution in axial, incompressible flow, obtained by Maruhn,[2] from a solution of the potential flow equations, is the same for elliptic profiles. The characteristic number A, specifying the peak velocity ratio, is changed, however. Thus

$$C_p = 1 - A^2 \sin^2\theta = 1 - (V/U_\infty)^2_{\max} \sin^2\theta \tag{1}$$

with

$$A = 1 + \delta \tag{2}$$

where $\delta = b/a$ is the profile slenderness ratio, b and a being, respectively, the minor and the major axes of the elliptic section. The angle θ is

$$\theta = \sin^{-1}\left(\frac{2\xi - \xi^2}{\delta^2 + (1-\delta^2)(2\xi - \xi^2)}\right)^{1/2} \tag{3}$$

being, as shown in the insert sketch in Fig. 1, the angle between the symmetry axis and the normal-to-the-profile contour. In

Received April 15, 1989; revision received Nov. 22, 1989.

*Aerodynamics Department (retired). Member AIAA.

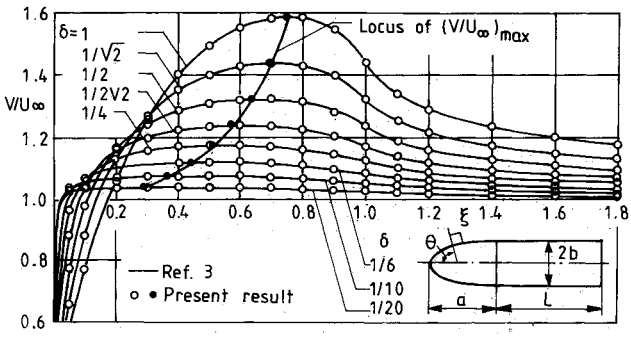

Fig. 1 Representation of velocity distributions on semi-infinite, two-dimensional bodies with elliptical noses.

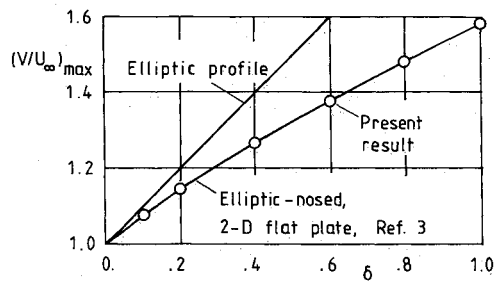

Fig. 2 Representation of peak velocity ratio vs nose slenderness ratio for elliptic profiles and semi-infinite, two-dimensional bodies with elliptical noses.

Eq. (3) the dimensionless variable $\xi = x/a$ is counted streamwise from the apex of the body.

Inserting $\delta = 1$ in Eq. (2) and Eq. (1) gives the classic solution for the circular cylinder in crossflow

$$C_p = 1 - 4\sin^2\theta \tag{4}$$

Semi-Infinite, Two-Dimensional Bodies with Elliptical Noses

By means of the comprehensive numerical results presented by Hess and Smith[3] for the velocity distribution on semi-infinite, two-dimensional bodies with elliptical noses, an extension of Eq. (1) has been constructed

$$C_p = 1 - \left[A - f(\tau)\delta^{5/4}\left(\frac{1}{3.53} + \frac{1}{7.5}\chi^5\right)\right]^2 \chi \tag{5}$$

where

$$\chi = \frac{\sin^2\theta}{\sin^2\theta_{\max}}, \qquad \chi \le 1 \tag{6}$$

$$f(\tau) = f\left(\frac{\tau - 1}{\tau}\right) = \begin{cases} 0 \text{ for } \tau = 1 \\ 1 \text{ for } \tau \to \infty \end{cases} \tag{7}$$

As in Ref. 1, the angle θ in Eq. (6) is normalized with respect to the length coordinate ξ_m for the peak velocity ratio on the nose. This coordinate is now

$$\xi_m = (2/3)\tan^{-1}[(A_\infty - 1)3]^{5/8} + 0.115 \tag{8}$$

with

$$A_\infty = 1 + \delta - (5/12)\delta^{5/4} \tag{9}$$

Again (as in Ref. 1), Eqs. (8) and (9) are empirical representations of the results presented by Hess and Smith.[3] Figure 2 shows $A_\infty = (V/U_\infty)_{\max}$ vs δ, and it is seen that the correlation with the numerical result[3] is very good. The factor $f(\tau)$ in Eqs. (5) and (7) is a correction for the influence of the afterbody length $\tau = L/a$ (see insert in Fig. 1) on the peak velocity ratio. The factor is zero for elliptic profiles and unity for semi-infinite bodies. For intermediate lengths of the afterbody, $1 < \tau < \infty$, the factor is not accurately known at present.

The velocity distribution for $\xi > \xi_m$, where ξ_m is defined by Eq. (8), is now represented by

$$\frac{V}{U_\infty} = (1 - C_p)^{1/2} = A_\infty - f(\tau)(A_\infty - 1) \times \frac{\Psi^3}{2 + \delta + \Psi^3 + (4.8 - \delta)\delta^{2/3}(\Psi - 1)^{7/4}} \tag{10}$$

where

$$\Psi = \frac{\xi - \xi_m}{1 - \xi_m}, \qquad \xi > \xi_m \tag{11}$$

Results and Discussion

The theoretical velocity distributions on semi-infinite, two-dimensional bodies with elliptical noses in symmetric, incompressible flow, presented by Hess and Smith,[3] can be represented by semiempirical expressions. Results for nose-slenderness ratios from 1/20 to 1 are shown in Fig. 1. The representation of the locus of the peak velocity ratio (solid symbols) by Eq. (8) is quite satisfactory.

The preceding result transformed into pressure coefficients is shown in Fig. 3 and thus represents a solution to the poten-

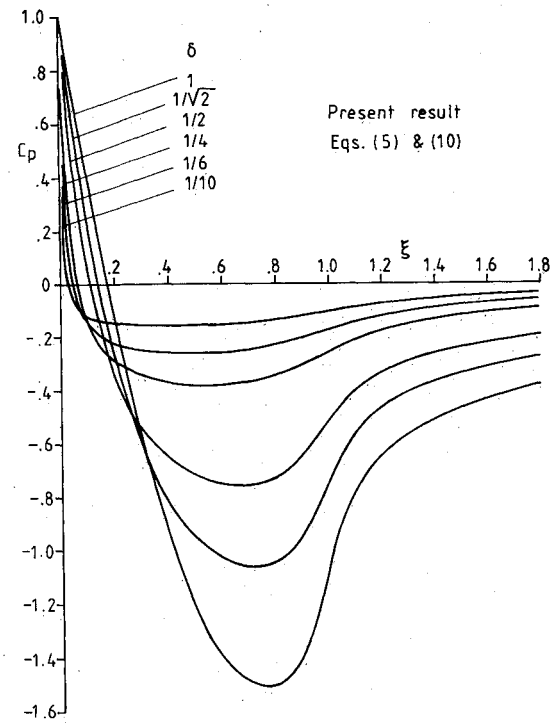

Fig. 3 Pressure coefficient distributions on semi-infinite, two-dimensional bodies with elliptical noses.

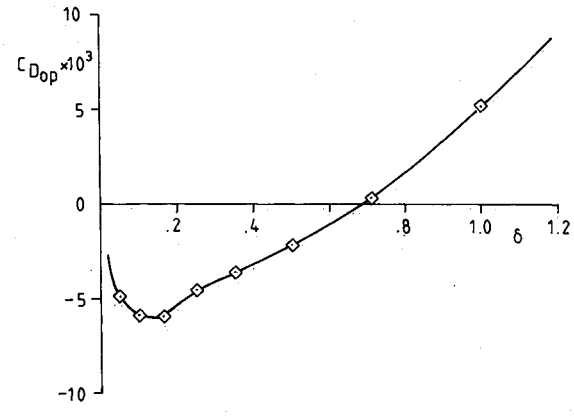

Fig. 4 Pressure drag coefficient vs nose slenderness ratio for semi-infinite, two-dimensional bodies with elliptical noses.

tial flow equations with the same degree of accuracy as that for the velocity distributions in Fig. 1.

The pressure distribution on the nose in situ on the two-dimensional slab has been integrated numerically in order to obtain the two-dimensional drag coefficient. The pressure drag coefficient vs the nose-slenderness ratio is shown in Fig. 4, and it is seen that an appreciable suction force is generated on the slender noses and that the drag coefficient increases for increasing slenderness ratio slightly more than linearly. (If the result is a realistic one, it cannot be judged at present. Suitable experimental data seem to be lacking.)

Conclusion

A semiempirical, analytical representation of the numerical solution to the incompressible potential flow equations for the pressure distribution on semi-infinite, two-dimensional bodies with elliptical noses has been obtained for nose slenderness ratios up to unity. The correlation with the theoretical result is very satisfactory. A strong dependence of the nose pressure drag coefficient on the nose-slenderness ratio is evident. Large suction forces are generated on the slender noses. The accuracy of the drag coefficient is not known at present.

Acknowledgment

This work was sponsored by the Material Administration of the Armed Forces, Air Material Department, Missiles Directorate, Sweden, under Contract AU-2157.

References

[1]Larson, E. S., "The Low Speed Pressure Distribution on Axi-symmetric Elliptic-Nosed Bodies," *Journal of Aircraft,* Vol. 25, No. 10, 1988, pp. 969–970.

[2]Maruhn, K., "Druckverteilungsrechnungen an Elliptischen Rümpfen und ihrem Aussenraum," *Jahrbuch 1941 der Deutschen Luftfahrtforschung,* pp. I135–I145.

[3]Hess, J. L., and Smith, A. M. O., "Calculation of Potential Flow about Arbitrary Bodies," *Progress in Aeronautical Sciences,* Vol. 8, Pergamon, Great Britain, 1967.

Cloud-to-Ground Strikes to the NASA F-106 Airplane

Vladislav Mazur*
NOAA/ERL/National Severe Storms Laboratory, Norman, Oklahoma 73069
and
Bruce D. Fisher†
NASA Langley Research Center, Hampton, Virginia 23665

Introduction

RETURN strokes of cloud-to-ground (CG) flashes are believed to represent the most severe lightning threat to aircraft. Peak current amplitudes for first return strokes (subsequent return strokes are weaker) determined from measurements at ground level have a median value in the range of 20–40 kA with 200 kA occurring at about the 1% level.[1] Current rates of rise derived from measured return stroke electric fields have an estimated mean maximum rise rate of about 1.8×10^{11} A s^{-1} for both first and subsequent strokes.[2] The Society of Automotive Engineers (SAE) recommends using a peak current value of 200 kA and a current rate of rise of 10^{11} A s^{-1} for aircraft lightning tests.[3] The validity of such a lightning threat to aircraft at altitude has been questioned. Direct measurements of return stroke current as a function of altitude do not exist. However, the variation of the current amplitude with height can be deduced by measuring the light intensity of the lightning channel, which is strongly correlated with return stroke current.[4]

This Note describes the CG strike data (20 cases) obtained with the NASA F-106B research airplane during the 1984–86 storm seasons in the vicinity of Wallops Island, Virginia.

Identification of a CG strike

In identifying strikes associated with CG flashes, we searched for a close coincidence, in both time and space, of return stroke channels and lightning attachments to the F-106B. The time and position of CG flashes were determined with the East Coast ground strike location network, which utilized magnetic direction finders manufactured by Lightning Location and Protection, Inc.[5] The airplane and network clocks were synchronized to the WWV time standard to an accuracy of 1 ms. The timing of a CG flash (time of the first return stroke) was recorded, however, to the nearest 10 ms. The moment of a strike attachment to the F-106B was identified by the onboard trigger signal. The position of the airplane in projection on the ground plane was obtained with a tracking C-band radar at Wallops Island.

An aircraft strike was considered to be associated with a CG flash if the range difference between the locations of the return stroke and the airplane during the attachment was within several tens of kilometers, and the associated time difference was less than 1 s. The range difference criterion is based on 1) the range accuracy of the CG locations provided by the ground-strike location network and 2) the range difference caused by the intracloud propagation of a CG flash within the time interval between attachment to the airplane and attachment to the ground. Location errors of an LLP system depend on the range of the flash from the direction finders and, to a lesser extent, on azimuthal angle. For distances typical of F-106B flights near Wallops Island (50–200 km), location errors may vary between 20 and 100 km.[6] A 10 ms time difference between airplane and ground attachment may correspond to a range difference of 1–1000 km depending on the type of lightning process that has taken place between attachments. The propagation speed varies between 10^5 and 10^8 ms^{-1} for different processes in the flash. For distances typical of flights and for the time differences between attachments (see the columns "Range" and "t" in Table 1), location errors are of several tens of kilometers. This is well within the range of distances between locations of attachment shown in column of "R" of Table 1.

The choice of the time difference criterion is based on lightning discharge durations, known to be more than several hundreds of milliseconds long.

Summary of CG Strikes to the F-106B During 1984-86 Seasons

During three thunderstorm seasons (1984–86), the NASA Storm Hazards Program was devoted to studying lightning strikes to aircraft in the lower altitude regions of thunderstorms. The most obvious altitude at which an aircraft may intercept a main part of the return stroke is below the cloud base. However, the probability of obtaining lightning strikes at such low altitudes decreases drastically, as shown in the analyses of the commercial airline data.[7] Therefore, attempted interceptions of the main return stroke channels

Presented as Paper 88-0390 at the AIAA 26th Aerospace Sciences Meeting, Reno, NV, Jan. 11–14, 1988; received May 11, 1989; revision received Sept. 15, 1989.

*Physicist.
†Research Engineer.